Article

# Penning-trap measurement of the $Q$ value of electron capture in $^{163}$Ho for the determination of the electron neutrino mass

**Christoph Schweiger** [1] ✉, **Martin Braß** [2,10], **Vincent Debierre** [1], **Menno Door** [1], **Holger Dorrer**[3], **Christoph E. Düllmann** [3,4,5], **Christian Enss** [6], **Pavel Filianin** [1], **Loredana Gastaldo** [6], **Zoltán Harman**[1], **Maurits W. Haverkort** [2], **Jost Herkenhoff** [1], **Paul Indelicato** [7], **Christoph H. Keitel** [1], **Kathrin Kromer** [1], **Daniel Lange** [1,8], **Yuri N. Novikov** [9], **Dennis Renisch** [3,4], **Alexander Rischka**[1], **Rima X. Schüssler** [1,11], **Sergey Eliseev**[1] & **Klaus Blaum** [1]

The investigation of the absolute scale of the effective neutrino mass remains challenging due to the exclusively weak interaction of neutrinos with all known particles in the standard model of particle physics. At present, the most precise and least-model-dependent upper limit on the electron antineutrino mass is set by the Karlsruhe Tritium Neutrino Experiment (KATRIN) from the analysis of the tritium β-decay. Another promising approach is the electron capture in $^{163}$Ho, which is under investigation using microcalorimetry by the Electron Capture in Holmium (ECHo) and HOLMES collaborations. An independently measured $Q$ value for this process is vital for the assessment of systematic uncertainties in the neutrino mass determination. Here we report a direct, independent determination of this $Q$ value by measuring the free-space cyclotron frequency ratio of highly charged ions of $^{163}$Ho and $^{163}$Dy in the Penning-trap experiment PENTATRAP. Combining this ratio with atomic physics calculations of the electronic binding energies yields a $Q$ value of $2{,}863.2 \pm 0.6$ eV $c^{-2}$, which represents a more than 50-fold improvement over the state of the art. This will enable the determination of the electron neutrino mass on a sub-electronvolt level from the analysis of the electron capture in $^{163}$Ho.

The observation of neutrino flavour oscillations proves that neutrinos are massive particles, establishing that the weak neutrino flavour eigenstates are a superposition of three neutrino mass eigenstates, in contradiction to the standard model of particle physics[1,2]. Oscillation experiments can only investigate the differences between the squared neutrino mass eigenvalues, leaving the absolute scale of the neutrino mass an open question. Thus, the absolute scale of the neutrino mass remains one of the most sought-after quantities in nuclear and particle physics, cosmology and theories beyond the standard model that could potentially explain the origin of the neutrino rest mass[3–6].

[1]Max-Planck-Institut für Kernphysik, Heidelberg, Germany. [2]Institute for Theoretical Physics, Heidelberg University, Heidelberg, Germany. [3]Department of Chemistry, Johannes Gutenberg-Universität Mainz, Mainz, Germany. [4]Helmholtz-Institut Mainz, Mainz, Germany. [5]GSI Helmholtzzentrum für Schwerionenforschung GmbH, Darmstadt, Germany. [6]Kirchhoff Institute for Physics, Heidelberg University, Heidelberg, Germany. [7]Laboratoire Kastler Brossel, Sorbonne Université, CNRS, ENS-PSL Research University, Collège de France, Campus Pierre et Marie Curie, Paris, France. [8]Heidelberg University, Heidelberg, Germany. [9]NRC 'Kurchatov Institute'–Petersburg Nuclear Physics Institute, Gatchina, Russia. [10]Present address: Institute of Solid State Physics, TU Wien, Vienna, Austria. [11]Present address: Van der Waals-Zeeman Institute, Institute of Physics, University of Amsterdam, Amsterdam, the Netherlands. ✉e-mail: christoph.schweiger@mpi-hd.mpg.de

Neutrinos are produced in weak nuclear decays; a model-independent measurement of their rest mass can be performed in a kinematic study of the decay products, where the neutrino itself is not directly detected. Relying on energy and momentum conservation, this is currently the most model-independent approach for neutrino mass determinations. Kinematic investigations constrain the effective rest mass of the electron neutrino (or antineutrino) $m_{\nu_e}^2 = \sum_{i=1}^{3} |U_{ei}|^2 m_i^2$, where $U_{fi}$ are the elements of the Pontecorvo–Maki–Nakagawa–Sakata matrix, which describes the superposition of mass eigenstates $m_i$ ($i \in \{1, 2, 3\}$) in the flavour eigenstates $\nu_f$ ($f \in \{e, \mu, \tau\}$). The individual mass eigenstates are not resolved in these experiments as the squared mass differences are well below current instrumental resolutions—the largest such difference is $\Delta m_{32}^2 = (2.453 \pm 0.033) \times 10^{-3}$ eV$^2$ $c^{-4}$ (ref. [7]).
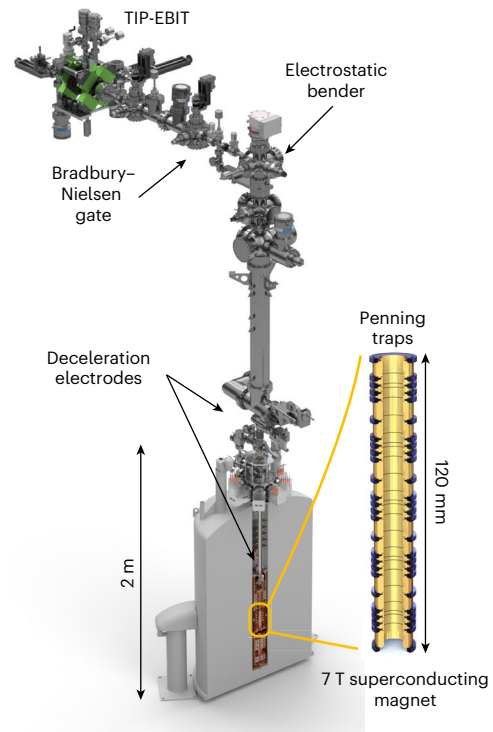
The most stringent constraint on the neutrino mass scale comes from the analysis of the matter distribution in the Universe, which provides a limit on the sum of the neutrino masses of <120 meV $c^{-2}$ (ref. [8]). The most stringent direct limit of 0.8 eV $c^{-2}$ (90% confidence level) from a kinematic study of tritium $\beta$-decay was set by the KATRIN collaboration[9,10].

Complementary to this approach, there are several experiments using calorimetric techniques to investigate the neutrino rest mass directly. The first calorimetric approaches were the MANU and MIBETA experiments investigating $^{187}$Re $\beta$-decay, yielding upper limits of 19 and 15 eV $c^{-2}$ (90% confidence level), respectively[11]. Two current experiments, ECHo[12,13] and HOLMES[14,15], are investigating the electron capture in $^{163}$Ho $\rightarrow$ $^{163}$Dy + $\nu_e$ + $E_{cal}$, where $E_{cal}$ is the energy detected in a calorimeter. The current upper limit of the electron neutrino rest mass is on a level of <150 eV $c^{-2}$ (ref. [13]) and the ECHo and HOLMES collaborations aim to achieve sensitivities well below <1 eV $c^{-2}$ (ref. [12]).

Within the ECHo collaboration, metallic magnetic calorimeters are used for the measurement of the energy of all emitted radiation, except for the energy carried away by the neutrino. This is obtained by implanting $^{163}$Ho ions directly into the absorber material of the detector. The calorimetrically measured decay spectrum is subsequently analysed by fitting it to a theoretical spectral shape from which the $Q$ value, as well as $m_{\nu_e}$, can be determined. To quantitatively investigate systematic effects in the interpretation of the calorimetrically measured spectra that might arise due to the $^{163}$Ho ions being implanted into a metallic material, this $Q$ value is best compared to one obtained from an independent direct measurement. The required accuracy of ~1 eV $c^{-2}$ can only be reached at present using high-precision Penning-trap mass spectrometry. In Penning-trap mass spectrometry, the $Q$ value is addressed directly through a measurement of the mass difference of the mother and daughter nuclides, $^{163}$Ho and $^{163}$Dy, respectively[12,16], by measuring the free-space cyclotron frequency ratio of the two species in a strong homogeneous magnetic field $B$. Within a magnetic field, an ion with charge-to-mass ratio $q/m$ is forced into a circular orbit, in which it revolves with the free-space cyclotron frequency $\nu_c = \frac{1}{2\pi} \frac{q}{m} B$. In a Penning trap, a superimposed weak quadrupolar electrostatic potential confines the ion along the magnetic field lines and modifies the ion's radial motion: the free-space cyclotron motion splits into the magnetron motion with a frequency $\nu_-$ and the modified cyclotron motion with a frequency $\nu_+$. The quadrupolar electrostatic potential also induces a harmonic oscillatory motion with frequency $\nu_z$ along the magnetic field lines. From a measurement of all three motional eigenfrequencies, the free-space cyclotron frequency can be reconstructed using the invariance theorem $\nu_c^2 = \nu_+^2 + \nu_z^2 + \nu_-^2$ (ref. [17]). From subsequent measurements of the free-space cyclotron frequency, the ratio $R_{q+} = \nu_c\left(^{163}\text{Dy}^{q+}\right) / \nu_c\left(^{163}\text{Ho}^{q+}\right)$ is determined, which finally allows the $Q$ value to be determined by including atomic physics calculations of the binding energy difference $\Delta E_B^{q+}$ of the removed electrons:

$$Q = m_{Dy}^{q+} \left(R_{q+} - 1\right) + \Delta E_B^{q+}. \qquad (1)$$

$\Delta E_B^{q+}$ is given by the difference in the sum of the binding energies of the $n$ missing electrons in the highly charged ions (HCIs) of both nuclides,



TIP-EBIT

Electrostatic bender

Bradbury–Nielsen gate

Deceleration electrodes

Penning traps

120 mm

2 m

7 T superconducting magnet

**Fig. 1 | Rendered overview of the PENTATRAP experimental set-up.** The upper horizontal part of the beamline is located on the ground floor, while the superconducting magnet is located in a dedicated laboratory in the basement. The TIP-EBIT is an electron beam ion trap specifically designed for very small samples sizes[21]. Following the TIP-EBIT in the horizontal beamline, a Bradbury–Nielsen gate is used to separate a single charge state. HCIs produced in the TIP-EBIT are guided through the electrostatic beamline to the stack of five identical Penning traps in the superconducting magnet. Deceleration electrodes with appropriately timed voltage pulses are used to capture the HCIs in the Penning traps. A more detailed view of the Penning-trap stack is shown on the right.

and $m_{Dy}^{q+}$ is the 'reference' mass of the HCI of dysprosium. $q = n \cdot e$ is the charge of the ions, where $e$ is the elementary charge and $n$ the number of removed electrons (charge state). To enhance the readability of formulae, sometimes $q$ also denotes the number of missing electrons $n$.
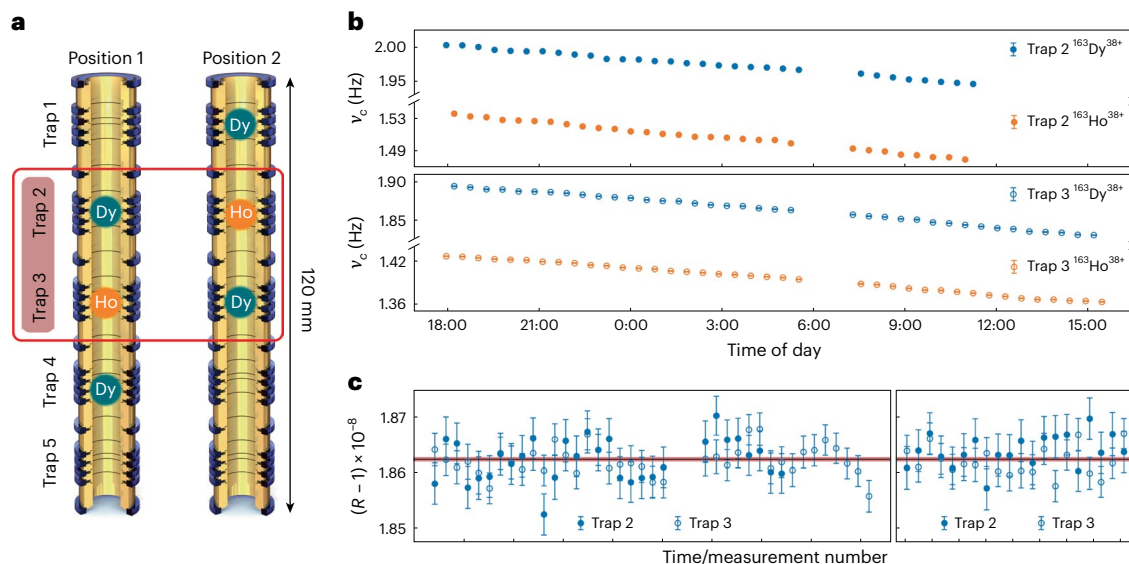
## The Penning-trap experiment PENTATRAP
### Experimental set-up

Measurements of $R$ of the two HCIs ($^{163}$Ho$^{q+}$ and $^{163}$Dy$^{q+}$) were carried out with the high-precision Penning-trap mass spectrometer PENTATRAP located at the Max-Planck-Institute for Nuclear Physics in Heidelberg, Germany[18,19]. An overview of the apparatus is given in Fig. 1.

HCIs of the synthetic radioisotope $^{163}$Ho, which was produced by neutron irradiation of stable $^{162}$Er (ref. [20]), and HCIs of the stable $^{163}$Dy were produced in a compact room-temperature electron beam ion trap (EBIT) that was specifically designed and constructed for the production of HCIs from samples available only in limited quantities (TIP-EBIT)[21]. For the measurements reported here only $2 \times 10^{15}$ atoms of $^{163}$Ho were used, with a typical sample containing about $10^{14}$ atoms of $^{163}$Ho. HCIs of the two species were extracted with a kinetic energy of 4.4 keV $q^{-1}$ from the EBIT and transported through an electrostatic beamline towards the Penning traps. Individual charge states $n = \{38, 39, 40\}$ were selected using a Bradbury–Nielsen Gate and a fast switching electronic circuit[22,23] located about 1.5 m from the EBIT. Just before reaching the mass spectrometer, the HCIs were decelerated to a few electronvolts per $q$ by appropriately timed voltage pulses on two cylindrical drift tubes.

The mass spectrometer consisted of a stack of five identical cylindrical Penning traps located in the cold bore of a 7 T actively

**Fig. 2 | Overview of the measurement procedure and resulting data structure.** **a**, Rendering of the stack of five identical cylindrical Penning traps of the PENTATRAP experiment. Traps 2 and 3, with labels marked in red, are used as measurement traps and are equipped with a detection system. Shuttling the ions from Position 1 into Position 2 effectively swaps the ion species in traps 2 and 3, resulting in the alternating data structure as shown in **b**. Traps 1 and 4 are used as storage traps, while trap 5 is not used in this measurement. **b**, Exemplary dataset of the measured $v_c$ of $^{163}$Ho (orange) and $^{163}$Dy (blue) in traps 2 (upper panel) and 3 (lower panel) for one measurement run in charge state $q = 38 \cdot e$. For traps 2 and 3 frequency offsets of 25,081,589 Hz and 25,081,620 Hz were subtracted. The linear drift of the free-space cyclotron frequency can be attributed to the slow decay of

the magnetic field of the superconducting magnet due to the flux creep effect[30,31]. Note that the $y$ axis is broken for illustrative purposes and that the error bars are smaller than the data point markers. **c**, $R_i$ of $v_c$ of $^{163}$Dy and $^{163}$Ho in traps 2 (filled circles) and 3 (empty circles) determined from the full dataset of two runs for the charge state $n = 38$. The data for each run are shown in separate panels; the ratios from **b** are shown in the left panel; the right panel shows ratios from the second dataset. The horizontal black line indicates the weighted average of all measured ratios for this charge state with the light red band marking the $1\sigma$ uncertainty band. Error bars correspond to the $1\sigma$ statistical uncertainty that is propagated by Gaussian uncertainty propagation.

shielded superconducting magnet[18,24]. The voltages applied to the Penning-trap electrodes were supplied by an ultrastable voltage source[25]. The Penning traps and the detection system were located inside a vacuum chamber immersed in liquid helium at a temperature of about 4 K. Two (trap 2 and trap 3; Fig. 2a) of the five Penning traps were equipped with a non-destructive image current detection system[18,26–28] and were used to measure the motional frequencies of the ions. Trap 1 and trap 4 served as storage traps, while trap 1 was also used as a capture trap when a new set of ions was loaded into the trap stack.

Environmental parameters affecting the magnetic field in the traps were stabilized (such as the temperature in the laboratory to 0.1 K/day and the liquid helium level and pressure of helium gas inside the cold bore of the magnet). In these conditions, the magnetic field exhibited a relative drift of a few $10^{-10}$ per hour[29]. Frequency measurements were performed overnight and on weekends, when external perturbations were minimal.

The measurement started with loading a set of three ions in the order $^{163}$Dy, $^{163}$Ho and $^{163}$Dy into traps 2, 3 and 4, respectively (Fig. 2a). The motional frequencies of the HCIs in traps 2 and 3 were measured simultaneously, starting with the ions in Position 1. Subsequently, the ions were shuttled to Position 2, which effectively swapped the ion species in traps 2 and 3 (Fig. 2a) and the measurement was repeated. The resulting data structure is shown in Fig. 2b where $v_c$ is plotted as a function of the measurement time. Alternating data points for $^{163}$Dy and $^{163}$Ho result from the swapping of the ion species in traps 2 and 3. More details of the ion preparation and the measurement sequence are given in the Methods.
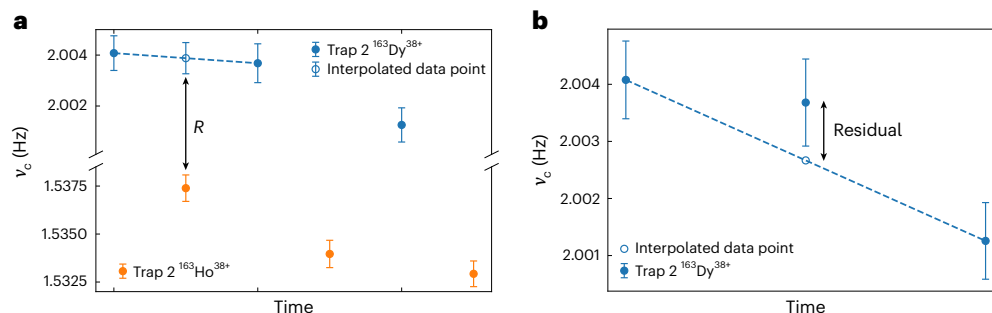
## Data analysis

To extract frequency ratios $R_i$ from $v_c$, the magnetic field behaviour is interpolated between the individual frequency measurement data

points from one species to the time when the other species' frequencies were measured.

Figure 2b shows exemplary the free-space cyclotron frequencies from one measurement run performed on ions with the charge state $q = 38 \cdot e$. The linear slope of the data points can be attributed to the slow decay of the magnetic field of the superconducting magnet due to the flux creep effect[30,31] and is on the order of a few $10^{-10}$ per hour relative to the absolute magnetic field of ~7 T.

In the data analysis, the frequency of $^{163}$Dy was linearly interpolated between two data points to the time at which $^{163}$Ho was measured. $R_i$ was determined from this interpolated data point, as illustrated in Fig. 3a. This procedure was followed for the full dataset. Residual nonlinear behaviour of the cyclotron frequency drift, originating from physical effects that alter the temperature and position of magnetic materials that surround the Penning traps and change the magnetic field within the traps, was taken into account in the uncertainty of the interpolated $R_i$. For this, the frequency data points were interpolated back to themselves (Fig. 3b), and the sum of the residuals divided by the number of residuals was included as an additional uncertainty in the ratio. The resulting ratios $R_i = v_{c,i}\left(^{163}\mathrm{Dy}^{38+}\right)/v_{c,i}\left(^{163}\mathrm{Ho}^{38+}\right)$ for the two measurement runs are shown in Fig. 2c for both traps. The ratios for the individual traps were consistent, therefore the final ratio was calculated as the weighted average and shown as a red line including the $1\sigma$ uncertainty band. For the calculation of the uncertainty of the final ratio, the inner error $\sigma_{int}^2$ and the outer error $\sigma_{ext}^2$ were calculated, and the larger of the two was used as the final uncertainty[32,33]:

$$\sigma_{int}^2 = \frac{1}{\sum_i \frac{1}{\sigma_i^2}} \tag{2}$$

**Fig. 3 | Illustration of the data analysis procedure.** Detailed plot of the first few datapoints of the cyclotron frequency $\nu_c$ from Fig. 2b to illustrate the data analysis procedure. From the frequency values, an offset of 25,081,589 Hz is subtracted. **a**, Linear interpolation between two $^{163}$Dy datapoints to the time at which $^{163}$Ho was measured for the determination of $R_i$. Note that the vertical axis was broken for illustration purposes. **b**, Exemplary estimation of the nonlinearity by interpolation of the data onto itself. Here we linearly interpolate between the first and third datapoints and determine the difference between the measured datapoint between and the interpolated one. The sum of these 'residuals' divided by the number of residuals in the full dataset is taken into account as an additional uncertainty of the ratio. For details of the analysis procedure see the main text. Error bars correspond to the $1\sigma$ statistical uncertainty that is propagated by Gaussian uncertainty propagation.

$$\sigma_{\text{ext}}^2 = \frac{\sum_i \frac{1}{\sigma_i^2}(R_i - \tilde{R})^2}{(N-1)\sum_i \frac{1}{\sigma_i^2}}. \tag{3}$$

Here, $R_i$ and $\sigma_i$ are individual cyclotron frequency ratios and their corresponding $1\sigma$ uncertainties, $\tilde{R}$ is the weighted average and $N$ is the total number of ratios.

The total systematic uncertainty (for example, field anharmonicities and inhomogeneity, image charge shift and relativistic shift) was strongly suppressed due to the fact that $^{163}$Ho and $^{163}$Dy in the same charge state form a unique mass doublet with a sufficiently small mass difference of about 2.8 keV. With a difference in the mass-to-charge ratio of only about $10^{-8}$, the same trapping potential was used for both $^{163}$Ho and $^{163}$Dy and the magnetron and axial frequencies were sufficiently equal. Thus, all systematic uncertainties in the free-space cyclotron frequency measurement cancelled to a large extent in the determination of $R$ and were smaller than $10^{-12}$. Extended Data Table 1 summarizes the considered systematic shifts. An additional systematic uncertainty can arise from the fact that HCIs might have long-lived low-energy atomic metastable states, as observed in previous measurements[34]. This is undesirable as it would shift the determined $Q$ value by the energy of the metastable state. In the 'Q value determination' section we compare the $Q$ values resulting from the measurements of three different charge states, which allowed us to exclude potential shifts in the $Q$ value due to long-lived electronic metastable states that would influence each charge state differently. The final ratios of free-space cyclotron frequencies of the ions in the different charge states are summarized in Table 2.

## Calculation of the binding energy differences

Theoretical calculations provided the binding energies of the electrons removed from the neutral Ho and Dy atoms. The Dy and Ho atoms are in the $[\text{Xe}]4f^{10}6s^2\,{}^5I_8$ and $[\text{Xe}]4f^{11}6s^2\,{}^4I_{15/2}$ electronic states, respectively. For better control of systematic effects, several HCI of Dy and Ho were considered in the experiment, namely, Dy$^{38+,39+,40+}$, with the ground states $[\text{Ar}]3d^{10,9,8}$, respectively, and Ho$^{38+,39+,40+}$ with ground states $[\text{Ar}]3d^{10}4s$, $[\text{Ar}]3d^{10}$ and $[\text{Ar}]3d^9$, respectively.

### Configuration interaction method

In a first set of calculations, the binding energies were calculated in Quanty[35–37] using the configuration interaction method. The starting point was a fully relativistic density functional theory calculation with the full-potential local-orbital minimum-basis code FPLO[38–40]. The density functional theory calculation determined the ground-state density of the ion around which a configuration interaction expansion was made. The corresponding Kohn–Sham orbitals were used as

**Table 1 | Summary of the electronic binding energy differences**

| q/e | $\Delta E_{\text{B,CI}}$ (eV) | $\Delta E_{\text{B,MCDHF}}$ (eV) | $\Delta E_{\text{B,MCDFGME}}$ (eV) | $\Delta E_{\text{B}}^{q+}$ (eV) |
|---|---|---|---|---|
| 38 | 38.8±1.0 | 36.5±0.8 | 38.1±1.5 | 37.4±1.4 |
| 39 | 1,148.2±1.0 | 1,146.7±0.8 | 1,148.1±1.5 | 1,147.3±0.7 |
| 40 | 1,116.6±1.0 | 1,115.1±0.8 | 1,116.4±1.5 | 1,115.7±0.7 |

The electronic binding energy differences are given for the three charge states from the three theory calculations: the configuration interaction (CI) method, the multiconfiguration Dirac–Hartree–Fock (MCDHF) method and the multiconfiguration Dirac–Fock general matrix elements (MCDFGME) method. The $1\sigma$ uncertainties are given for each. The final $\Delta E_{\text{B}}$ for the determination of the $Q$ value (right column) were calculated as the weighted average of the configuration interaction and MCDHF methods.

single-particle bases to construct the Slater determinants that span a configuration space. The Hamiltonian comprises Coulomb and static Breit interactions between the electrons, as well as their relativistic kinetic energies and potential energies due to Coulomb attraction of the ion's nucleus. Diagonalization of this Hamiltonian on a given configuration space using the Lánczos algorithm determined the ground-state energy of an ion.

At first, only the space of the ground-state configuration was considered. The configuration space was then iteratively expanded to include single, double and triple excitations of electrons into orbitals with higher principal quantum numbers. Details of these calculations are given in the Methods. We obtained the calculated binding energy differences given in Table 1.

### MCDHF method

In the second set of calculations, we used the MCDHF method[41] combined with Brillouin–Wigner many-body perturbation theory[42,43].

In the MCDHF method, the atomic state function is modelled as a superposition of configuration state functions (CSFs) with fixed angular momentum, magnetic and parity quantum numbers. The CSFs are built as Slater determinants of Dirac orbitals in the $jj$ coupling scheme. Using the parallel GRASP2018 codes[43], we expanded the space of virtual orbitals used for the construction of CSFs by single- and double-electron exchanges in a systematic manner. The convergence of the energies with respect to the maximal principal quantum number of virtual orbitals was monitored, and the spread of values resulting from different correlation models was used as a measure of the leading contribution (90%) of the theoretical uncertainties. In case of the HCI, the set of CSFs was generated with exchanges including all occupied orbitals from $1s$ onwards, and with virtual orbitals up to typically $10h$. Virtual orbitals were optimized in a layer-by-layer fashion[43,44].

**Table 2 | Summary of the main results**

| q/e | R | δR | $\Delta E_B^{q+}$ (eV) | Q (eV c$^{-2}$) |
|-----|---|-----|------|------|
| 38 | 1.000000018623 | 3.0×10$^{-12}$ | 37.4±1.4 | 2,863.4±1.5 |
| 39 | 1.000000011307 | 4.1×10$^{-12}$ | 1,147.3±0.7 | 2,863.2±0.9 |
| 40 | 1.000000011516 | 3.5×10$^{-12}$ | 1,115.7±0.7 | 2,863.2±0.9 |

Weighted averages of the ratios and their uncertainties, weighted averages of the binding energy differences (see Table 1) and the calculated Q values are given for the three measured charge states. 1σ uncertainties are listed.

The effects of the Breit interaction, recoil and approximate quantum electrodynamic corrections were accounted for by the configuration interaction method using orbitals from the MCDHF procedure[43]. More details are given in the Methods. We obtained the theoretical binding energy differences listed in Table 1.

In a third set of calculations, we used the MCDFGME code[45] to check the previous results. The calculation was performed in the optimized level mode, where all correlation orbitals are fully relaxed instead of the layer-by-layer method. Convergence was much more difficult in this case and limited the number of extra orbitals that could be added in the evaluation of correlation. In this calculation, the magnetic and retardation interaction at the Breit level were included in the Dirac–Fock equations on the same footing as the Coulomb interaction, meaning that the Breit interaction was included to all orders in the correlation energy[46]. The Uehling potential was also evaluated to all orders[47]. Finally, self-energy screening was calculated using both the Welton method[48] and the model operator method[49]. For the HCIs, energies obtained by exciting occupied orbitals from $3s$ or $3d$ to open shells ($4f$, $6p$, $5d$, $7s$, $7p$ and $5g$) were compared. For neutrals, values obtained by exciting the core from $3d$ and $4s$ were compared. Calculations included only single and double excitations, as triple excitations led to unmanageably large numbers of magnetic and retardation integrals. All possible single excitations were included, even those obeying Brillouin's theorem[45]. The results are given in Table 1 and are in good agreement with the GRASP2018 evaluation. Both sets of values are in agreement with the uncorrelated values[50], confirming the good compensation of correlation between the two ions.

#### Final values for the binding energy difference
The final binding energy $\Delta E_B^{q+}$ for each charge state $q$ was calculated as the weighted average of the values from the configuration interaction and MCDHF calculations (Table 1). The uncertainty was determined by comparing the inner and outer errors and using the larger as the final uncertainty on $\Delta E_B^{q+}$. For the charge states $q = \{39, 40\} \cdot e$, the larger of the two uncertainties was averaged with the uncertainty assuming correlations between the configuration interaction and MCDHF methods; that is, with the uncertainty of 0.8 eV of the MCDHF method. The resulting $\Delta E_B^{q+}$ are consistent with the MCDFGME calculations described above, as well as with the calculations recently published in ref. 51.

### Q value determination
The Q value of the electron capture in $^{163}$Ho was determined from the measured R (see 'The Penning-trap experiment') and the theoretically calculated binding energy differences $\Delta E_B^{q+}$ (see 'Calculation of the binding energy differences' and Table 1) for each charge state $q = \{38, 39, 40\} \cdot e$ according to equation (1). The (reference) mass $m_{Dy}^{q+}$ of $^{163}$Dy$^{q+}$ was calculated starting from the mass of atomic $^{163}$Dy, $m_{Dy}$ (ref. 52) and subtracting the masses of the $n$ missing electrons[53,54] and their binding energies[55]. Table 2 lists R for the three measured charge states, as well as the 1σ uncertainty δR, which was computed using standard Gaussian uncertainty propagation.

Using equation (1) and the binding energy differences, the final Q values were calculated for the three charge states and are summarized in Table 2.
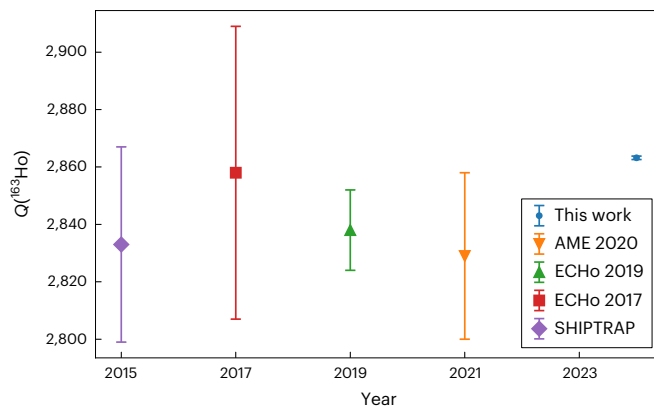


**Fig. 4 | Comparison of the most recent measurements of the $^{163}$Ho Q value.** Data from Penning-trap mass spectrometry (SHIPTRAP[56] and this work), microcalorimetry (ECHo 2017[57] and ECHo 2019[13]) and the most recent AME adjustment (AME 2020)[52] are shown. Error bars correspond to 1σ combined uncertainties.

The resulting Q values agree within their 1σ uncertainties. Resulting from this very good agreement, systematic deviations from either the free-space cyclotron ratio measurement or from the calculation of the binding energy difference can largely be excluded. Furthermore, the influence of unknown metastable electronic states can also largely be ruled out as it is very unlikely that an electronic metastable state would have exactly the same excitation energy in all three of the measured charge states.

The final Q value was calculated as the weighted average of the Q values obtained for the three charge states resulting in:

$$Q = 2{,}863.2 \pm 0.6 \text{ eV } c^{-2}. \qquad (4)$$

This value is in 1σ agreement with the previously measured value at SHIPTRAP of $2{,}833 \pm 34$ eV $c^{-2}$ (ref. 56), but 50 times more precise. In Fig. 4 the most recent measurements of the Q value of $^{163}$Ho from cryogenic microcalorimetry, Penning-trap mass spectrometry and the Atomic Mass Evaluation (AME) 2020 (ref. 52) are shown. The value from AME 2020 is an average from three different microcalorimetric measurements. Our value is slightly higher than the current AME adjustment, and agrees within 1.2σ.

The $^{163}$Ho electron capture Q value was obtained by combining a high-precision measurement of the free-space cyclotron frequency of HCIs of the mother and daughter nuclides in a Penning trap and precise atomic physics calculations of the electronic binding energies of the missing electrons. Experiments investigating the electron neutrino mass by microcalorimetric measurements of the decay spectrum of $^{163}$Ho such as those performed by the ECHo and HOLMES collaborations are now provided with an independently measured Q value with a precision of 0.6 eV, which allows the assessment of systematic uncertainties in the neutrino mass determination using cryogenic microcalorimetry on a level of <1 eV.

### Online content
Any methods, additional references, Nature Portfolio reporting summaries, source data, extended data, supplementary information, acknowledgements, peer review information; details of author contributions and competing interests; and statements of data and code availability are available at https://doi.org/10.1038/s41567-024-02461-9.

### References
1. Fukuda, Y. et al. Evidence for oscillation of atmospheric neutrinos. *Phys. Rev. Lett.* **81**, 1562–1567 (1998).
2. Ahmad, Q. R. et al. Direct evidence for neutrino flavor transformation from neutral-current interactions in the Sudbury Neutrino Observatory. *Phys. Rev. Lett.* **89**, 011301 (2002).

3. King, S. F. Neutrino mass models. *Rep. Progr. Phys.* **67**, 107–157 (2003).

4. Drexlin, G., Hannen, V., Mertens, S. & Weinheimer, C. Current direct neutrino mass experiments. *Adv. High Energy Phys.* **2013**, 293986 (2013).

5. Formaggio, J. A., de Gouvêa, A. L. C. & Robertson, R. G. H. Direct measurements of neutrino mass. *Phys. Rep.* **914**, 1–54 (2021).

6. de Gouvêa, A. Neutrino mass models. *Annu. Rev. Nucl. Part. Sci.* **66**, 197–217 (2016).

7. Group, P. D. et al. Review of particle physics. *Progr. Theor. Exp. Phys.* **2022**, 083C01 (2022).

8. Planck Collaboration Planck 2018 results—VI. Cosmological parameters. *Astron. Astrophys.* **641**, A6 (2020).

9. Aker, M. et al. The design, construction, and commissioning of the KATRIN experiment. *J. Instrum.* **16**, T08015 (2021).

10. Aker, M. et al. Direct neutrino-mass measurement with sub-electronvolt sensitivity. *Nat. Phys.* **18**, 160–166 (2022).

11. Nucciotti, A. The use of low temperature detectors for direct measurements of the mass of the electron neutrino. *Adv. High Energy Phys.* **2016**, 9153024 (2016).

12. Gastaldo, L. et al. The electron capture in $^{163}$Ho experiment–ECHo. *Euro. Phys. J. Spec. Top.* **226**, 1623–1694 (2017).

13. Velte, C. et al. High-resolution and low-background $^{163}$Ho spectrum: interpretation of the resonance tails. *Euro. Phys. J. C* **79**, 1026 (2019).

14. Faverzani, M. et al. The HOLMES experiment. *J. Low Temp. Phys.* **184**, 922–929 (2016).

15. Nucciotti, A. et al. Status of the HOLMES experiment to directly measure the neutrino mass. *J. Low Temp. Phys.* **193**, 1137–1145 (2018).

16. Eliseev, S., Novikov, Y. N. & Blaum, K. Penning-trap mass spectrometry and neutrino physics. *Annal. Physik* **525**, 707–719 (2013).

17. Brown, L. S. & Gabrielse, G. Geonium theory: physics of a single electron or ion in a Penning trap. *Rev. Mod. Phys.* **58**, 233–311 (1986).

18. Repp, J. et al. PENTATRAP: a novel cryogenic multi-Penning-trap experiment for high-precision mass measurements on highly charged ions. *Appl. Phys. B* **107**, 983–996 (2012).

19. Filianin, P. et al. Direct Q-value determination of the $\beta^-$ decay of $^{187}$Re. *Phys. Rev. Lett.* **127**, 072502 (2021).

20. Dorrer, H. et al. Production, isolation and characterization of radiochemically pure $^{163}$Ho samples for the ECHo-project. *Radiochim. Acta* **106**, 535–547 (2018).

21. Schweiger, C. et al. Production of highly charged ions of rare species by laser-induced desorption inside an electron beam ion trap. *Rev. Sci. Instrum.* **90**, 123201 (2019).

22. Bradbury, N. E. & Nielsen, R. A. Absolute values of the electron mobility in hydrogen. *Phys. Rev.* **49**, 388–393 (1936).

23. Schweiger, C. et al. Fast silicon carbide MOSFET based high-voltage push-pull switch for charge state separation of highly charged ions with a Bradbury-Nielsen gate. *Rev. Sci. Instrum.* **93**, 094702 (2022).

24. Roux, C. et al. The trap design of PENTATRAP. *Appl. Phys. B* **107**, 997–1005 (2012).

25. Böhm, C. et al. An ultra-stable voltage source for precision Penning-trap experiments. *Nucl. Instrum. Methods Phys. Res. Sect. A* **828**, 125–131 (2016).

26. Wineland, D. J. & Dehmelt, H. G. Principles of the stored ion calorimeter. *J. Appl. Phys.* **46**, 919–930 (1975).

27. Feng, X., Charlton, M., Holzscheiter, M., Lewis, R. A. & Yamazaki, Y. Tank circuit model applied to particles in a Penning trap. *J. Appl. Phys.* **79**, 8–13 (1996).

28. Nagahama, H. et al. Highly sensitive superconducting circuits at ~700 kHhz with tunable quality factors for image-current detection of single trapped antiprotons. *Rev. Sci. Instrum.* **87**, 113305 (2016).

29. Kromer, K. et al. High-precision mass measurement of doubly magic $^{208}$Pb. *Euro. Phys. J. A* **58**, 202 (2022).

30. Anderson, P. W. Theory of flux creep in hard superconductors. *Phys. Rev. Lett.* **9**, 309–311 (1962).

31. Anderson, P. W. & Kim, Y. B. Hard superconductivity: theory of the motion of Abrikosov flux lines. *Rev. Mod. Phys.* **36**, 39–43 (1964).

32. Nagy, S., Blaum, K. & Schuch, R. in *Lecture Notes in Physics: Trapped Charged Particles and Fundamental Interactions* Vol. 749 (eds Herfurth, F. & Blaum, K.) 1–36 (Springer, 2008).

33. Birge, R. T. The calculation of errors by the method of least squares. *Phys. Rev.* **40**, 207–227 (1932).

34. Schüssler, R. X. et al. Detection of metastable electronic states by Penning trap mass spectrometry. *Nature* **581**, 42–46 (2020).

35. Haverkort, M. W., Zwierzycki, M. & Andersen, O. K. Multiplet ligand-field theory using Wannier orbitals. *Phys. Rev. B* **85**, 165113 (2012).

36. Haverkort, M. W. et al. *Quanty* (Quanty, 2022); http://www.quanty.org

37. Braβ, M. & Haverkort, M. W. Ab initio calculation of the electron capture spectrum of $^{163}$Ho: Auger–Meitner decay into continuum states. *New J. Phys.* **22**, 093018 (2020).

38. Koepernik, K. & Eschrig, H. Full-potential nonorthogonal local-orbital minimum-basis band-structure scheme. *Phys. Rev. B* **59**, 1743–1757 (1999).

39. Opahle, I., Koepernik, K. & Eschrig, H. Full-potential band-structure calculation of iron pyrite. *Phys. Rev. B* **60**, 14035–14041 (1999).

40. Eschrig, H., Richter, M. & Opahle, I. in *Relativistic Electronic Structure Theory* Theoretical and Computational Chemistry Vol. 14 (ed. Schwerdtfeger, P.) 723–776 (Elsevier, 2004).

41. Grant, I. P. Relativistic calculation of atomic structures. *Adv. Phys.* **19**, 747–811 (1970).

42. Kotochigova, S., Kirby, K. P. & Tupitsyn, I. I. Ab initio fully relativistic calculations of X-ray spectra of highly charged ions. *Phys. Rev. A* **76**, 052513 (2007).

43. Fischer, C. F., Gaigalas, G., Jönsson, P. & Bieroń, J. GRASP2018—a Fortran 95 version of the general relativistic atomic structure package. *Comput. Phys. Commun.* **237**, 184–187 (2019).

44. Fischer, C. F., Godefroid, M., Brage, T., Jönsson, P. & Gaigalas, G. Advanced multiconfiguration methods for complex atoms: I. Energies and wave functions. *J. Phys. B* **49**, 182004 (2016).

45. Indelicato, P., Lindroth, E. & Desclaux, J. P. Nonrelativistic limit of Dirac-Fock codes: the role of Brillouin configurations. *Phys. Rev. Lett.* **94**, 013002 (2005).

46. Indelicato, P. Projection operators in multiconfiguration Dirac-Fock calculations: application to the ground state of helium-like ions. *Phys. Rev. A* **51**, 1132–1145 (1995).

47. Indelicato, P. Nonperturbative evaluation of some QED contributions to the muonic hydrogen $n=2$ Lamb shift and hyperfine structure. *Phys. Rev. A* **87**, 022501 (2013).

48. Indelicato, P., Gorveix, O. & Desclaux, J. P. Multiconfigurational Dirac-Fock studies of two-electron ions. II. Radiative corrections and comparison with experiment. *J. Phys. B* **20**, 651–663 (1987).

49. Shabaev, V. M., Tupitsyn, I. I. & Yerokhin, V. A. Model operator approach to the Lamb shift calculations in relativistic many-electron atoms. *Phys. Rev A.* **88**, 012513 (2013).

50. Rodrigues, G. C., Indelicato, P., Santos, J. P., Patté, P. & Parente, F. Systematic calculation of total atomic energies of ground state configurations. *Atom. Data Nucl. Data Tables* **86**, 117–233 (2004).

51. Savelyev, I. M., Kaygorodov, M. Y., Kozhedub, Y. S., Tupitsyn, I. I. & Shabaev, V. M. Calculations of the binding-energy differences for highly-charged Ho and Dy ions. *JEPT Lett.* **118**, 87–91 (2023).

52. Wang, M., Huang, W. J., Kondev, F. G., Audi, G. & Naimi, S. The AME 2020 atomic mass evaluation (II). Tables, graphs and references. *Chinese Phys. C* **45**, 030003 (2021).

53. Tiesinga, E., Mohr, P. J., Newell, D. B. & Taylor, B. N. CODATA recommended values of the fundamental physical constants: 2018. *Rev. Mod. Phys.* **93**, 025010 (2021).

54. Sturm, S. et al. High-precision measurement of the atomic mass of the electron. *Nature* **506**, 467–470 (2014).

55. Kramida, A. et al. *NIST Atomic Spectra Database* v.5.9 (NIST, 2021); https://physics.nist.gov/PhysRefData/ASD/ionEnergy.html

56. Eliseev, S. et al. Direct measurement of the mass difference of $^{163}$Ho and $^{163}$Dy solves the $Q$-value puzzle for the neutrino mass determination. *Phys. Rev. Lett.* **115**, 062501 (2015).

57. Ranitzsch, P. C.-O. et al. Characterization of the $^{163}$Ho electron capture spectrum: a step towards the electron neutrino mass determination. *Phys. Rev. Lett.* **119**, 122501 (2017).

## Methods

### Measurement preparation and sequence

The measurement preparation started with loading a set of three ions, in the order $^{163}$Dy, $^{163}$Ho and $^{163}$Dy into traps 2, 3 and 4, respectively (Fig. 2a). Each HCI was first loaded into trap 2, where its motional amplitudes were reduced by resistive cooling[17,58]. Great care was taken to ensure that only a single HCI was captured in a trap and cooled. For this also the 'magnetron cleaning' technique was applied[59]. After being prepared in this way, the ions were moved to one of the following traps and stored until the set of ions for a given measurement was complete.

In both measurement traps (traps 2 and 3), the motional frequencies of the HCIs were measured using the single-dip, double-dip and pulse-and-phase techniques[58,60]. The magnetron frequency was small compared with the other two motional frequencies and depends only very weakly on the ion's mass; it was therefore measured only once a day using the double-dip technique before the main measurement sequence. Thus, the main measurement sequence reduced to a measurement of the modified cyclotron frequency (pulse-and-phase technique) and the axial frequency (double-dip technique), which were performed simultaneously in traps 2 and 3. Compared with a single-trap measurement, this effectively doubled the statistics and furthermore allowed different analysis methods to be employed, as well as systematic checks through comparing the results obtained in both traps.

In the pulse-and-phase cycle, the starting phase of the cyclotron motion was set by exciting it using a dipolar pulse with the frequency determined with the double-dip method during the preparation. The modified cyclotron motion then evolved freely during the phase evolution time $T_{evol}$ (about 40 s) while the axial frequency was determined using a dip measurement[19,29,61–64]. Following the phase evolution time, the phase information that accumulated in the modified cyclotron motion was coupled to the axial motion using a π pulse on the sideband frequency and the final phase was measured with the image current detection system[60]. This is done in traps 2 and 3, starting with the ions in Position 1. Subsequently, the ions were shuttled to Position 2, which effectively swapped the ion species in traps 2 and 3 and the measurement was repeated (Fig. 2a). This sequence was repeated 24 times in one main measurement loop and can be continued, in principle, infinitely. Typically, the measurement is stopped due to either external magnetic field perturbations or charge exchange of the HCIs. Lifetimes of the HCIs until a charge exchange process happens were up to 36 hours. Reloading ions is beneficial as it allows one to compare different sets of ions, and therefore also systematic checks for contaminant ions that might be present in the Penning traps during the measurement or for possible metastable electronically excited states in the HCIs[34].

### Convergence studies with the configuration interaction and multiconfiguration Dirac–Fock methods

In the configuration interaction calculations made with the Quanty code, we iteratively expanded the configuration space with single, double and triple excitations into single-electron states with higher principal quantum numbers. For the ions this implies iterative inclusion of excitations into orbitals with $n = 4, 5, 6, 7, 8$, and for the neutral atom $n = 5, 6$.

The evolution of the ground-state energy with expanding configuration space was monitored and showed to good approximation $1/n$ behaviour that allowed extrapolation of the ground-state energy to estimate its uncertainty due to a truncated configuration space. Considering further uncertainties due to numerical accuracy, the choice of single-particle basis sets and triple excitations, we arrived at a total uncertainty of 1 eV for the estimation of the differences in binding energies of Ho$^{q+}$ and Dy$^{q+}$.

As consistency check, for every step where the configuration space was increased the binding energy difference between Ho$^{q+}$ and Dy$^{q+}$ was calculated. It showed an approximate $1/n^2$ behaviour, which

again allowed extrapolation. Within our uncertainties, we obtained the same results as in Table 1.

In case of the multiconfiguration Dirac–Fock calculations with the GRASP2018 package, as described in the main text, we found that for neutral atoms, the inclusion of all spectroscopic orbitals into the active space would lead to several tens of millions of CSFs, which is not tractable at present. For these systems, we included exchanges from the 3$s$ orbital up to typically 8$h$. To bridge the different models used for the neutral atoms and the HCIs, we also studied the intermediate Pd-like HCIs Dy$^{20+}$ and Ho$^{21+}$, with excitations from the 2$s$ orbital to typically 10$h$. We observed that the correlation terms largely cancelled in energy differences such as $[E(\text{Ho}) - E(\text{Ho}^{21+})] - [E(\text{Dy}) - E(\text{Dy}^{20+})]$ and $[E(\text{Ho}^{21+}) - E(\text{Ho}^{40+})] - [E(\text{Dy}^{20+}) - E(\text{Dy}^{40+})]$ due to the structural similarities of nearby charge states. These differences converged more quickly when the set of virtual orbitals was extended than with the individual energies $E(\text{Ho})$ and $E(\text{Dy})$ of the neutral atoms. We note that this inclusion of an intermediate system was useful because of the high charge states 38+, 39+ and 40+ in the experiment, and allowed uncertainties to be reduced.

## Data availability

Datasets generated during the current study are available from the corresponding author on reasonable request.

## Code availability

Code used in the analysis of the data is available from the corresponding author on reasonable request.

## References

58. Cornell, E. A., Weisskoff, R. M., Boyce, K. R. & Pritchard, D. E. Mode coupling in a Penning trap: π pulses and a classical avoided crossing. *Phys. Rev. A* **41**, 312–315 (1990).
59. Heiße, F. et al. High-precision mass spectrometer for light ions. *Phys. Rev. A* **100**, 022518 (2019).
60. Cornell, E. A. et al. Single-ion cyclotron resonance measurement of M(CO$^+$)/M(N$_2^+$). *Phys. Rev. Lett.* **63**, 1674–1677 (1989).
61. Rischka, A. et al. Mass-difference measurements on heavy nuclides with an eV/c$^2$ accuracy in the PENTATRAP spectrometer. *Phys. Rev. Lett.* **124**, 113001 (2020).
62. Ketter, J. et al. Classical calculation of relativistic frequency-shifts in an ideal Penning trap. *Int. J. Mass Spectrom.* **361**, 34–40 (2014).
63. Ketter, J., Eronen, T., Höcker, M., Streubel, S. & Blaum, K. First-order perturbative calculation of the frequency-shifts caused by static cylindrically-symmetric electric and magnetic imperfections of a Penning trap. *Int. J. Mass Spectrom.* **358**, 1–16 (2014).
64. Schuh, M. et al. Image charge shift in high-precision Penning traps. *Phys. Rev. A* **100**, 023411 (2019).

## Author contributions

## Funding

## Competing interests

The authors declare no competing interests.

## Additional information

**Extended data** is available for this paper at https://doi.org/10.1038/s41567-024-02461-9.

**Correspondence and requests for materials** should be addressed to Christoph Schweiger.

**Peer review information** *Nature Physics* thanks Pascal Quinet and the other, anonymous, reviewer(s) for their contribution to the peer review of this work.

**Reprints and permissions information** is available at www.nature.com/reprints.

**Extended Data Table 1 | Overview of the considered systematic shifts**

| Systematic shift | Magnitude |
|---|---|
| Relativistic shift | $\delta R < 10^{-12}$ [62] |
| Field anharmonicities/imperfections | $\delta R < 10^{-13}$ [24, 63] |
| Image charge shift | $\delta R < 10^{-13}$ [24, 64] |
| Dip lineshape | $\delta R < 10^{-13}$ |
| $C_1 B_1$ | Effect cancels in the ratio. |
| $C_1 C_3$ | Effect cancels in the ratio. |

Overview of the considered systematic shifts $\delta R$ in the determination of the frequency ratio $R$. $C_1$ and $C_3$ are Taylor expansion coefficients of the electrostatic trap potential and $B_1$ is the linear coefficient in a similar expansion of the magnetic field. The relativistic shift was estimated assuming conservatively that both radii agree within 1%.